Enhanced Active Power Transfer and Stability for Grid-Following Inverters Within an Ultraweak Grid

Guangda Ma, *Student Member, IEEE*, Chuan Xie, *Senior Member, IEEE*, Cheng Li, *Student Member, IEEE*, and Jianxiao Zou, *Member, IEEE*

***Abstract*—Grid-following (GFL) inverters face both severe large-signal destabilization (LSD) and small-signal destabilization risks in ultraweak grids. To address the LSD risk, this article reveals the effect of reactive current injection (RCI) on the power-angle property, terminal voltage, and maximum transferable active power (MTAP) in the presence of different short-circuit ratio (SCR) conditions. Then, the feasible ranges for active power and RCI are developed to prevent LSD and terminal voltage violation. By excluding the possibility of LSD with an enhanced MTAP, the small-signal stability of the GFL inverter is ensured by applying the impedance stability criteria. In this article, an optimization problem with constraints of internal and external stabilities is established to redesign the gains of the current controller, without requiring real-time detection during the solution process. The redesigned gains effectively ensure the small-signal stability of the GFL inverter while keeping a relatively high phase-locked loop (PLL) bandwidth in an ultraweak grid with SCR = 1.1, which is lower than that achieved by state-of-the-art methods. Finally, the simulation and experimental results confirm the effectiveness of the proposed guideline.**

***Index Terms*—Current controller design, grid-following inverter, stability, ultraweak grid.**

I. Introduction

DUE to their superior controllability and high-quality power, grid-following (GFL) inverters are still mainly power transfer interfaces for renewable energy resources integrated into the power grid [1]. However, GFL inverters suffer from both instability issues and limited active power transfer capacity, especially in weak grid conditions having a low short-circuit ratio (SCR) [2], [3]. To ensure the stable operation of the inverter-grid system in weak grids, both system operators and academic communities are working to tackle these unstable issues, and representative works are compared and summarized in Table I.

Received 17 June 2025; revised 4 September 2025 and 29 November 2025; accepted 7 January 2026. Date of publication 12 January 2026; date of current version 20 March 2026. This work was supported by the National Natural Science Foundation of Sichuan Province under Grant 2024NSFSC0118. Recommended for publication by Associate Editor H. Wu. *(Corresponding author: Chuan Xie.)*

Guangda Ma and Cheng Li are with the School of Automation Engineering, University of Electronic Science and Technology of China, Chengdu 611731, China (e-mail: gdma@std.uestc.edu.cn; chengli@std.uestc.edu.cn).

Chuan Xie and Jianxiao Zou are with the School of Automation Engineering, Shenzhen Institute for Advanced Study, University of Electronic Science and Technology of China, Chengdu 611731, China (e-mail: c.xie@uestc.edu.cn; jxzou@uestc.edu.cn).

Color versions of one or more figures in this article are available at https://doi.org/10.1109/TPEL.2026.3652852.

Digital Object Identifier 10.1109/TPEL.2026.3652852

The small-signal stability analysis of GFL inverters focuses on their dynamic performances when small disturbances occur in the input signals of the control part [4]. During the dynamic process, a phase difference occurs in the phase-locked loop (PLL) between the actual grid phase and the simulated control one. This will result in the negative admittance characteristics of the PLL added to the inverter output admittance [5], [6]. According to impedance stability criteria, the inverter-grid system will destabilize if the intersection frequency between the inverter and grid appears in the low-frequency negative real-part admittance range [7]. Based on these insights, small-signal destabilization (SSD) is characterized by the divergence of the PLL output signal along with severe low-frequency oscillations [8], [9], [10].

One simple way to improve the small-signal stability of GFL inverters is to limit the PLL bandwidth, but this degrades dynamic performance [11]. Another improvement in the PLL scheme is modifying its control structure, such as introducing an extra filter for reshaping the admittance characteristics of the PLL [9], [12]. However, the reconstruction of PLL in the existing inverters is troublesome and impractical [4]. To circumvent this limitation, an active damper is presented in [13] to mitigate the small-signal instability issue by an extra inverter connecting to the point of common coupling (PCC). However, this approach increases both the cost and the implementation complexity of the system. Furthermore, some studies focus on reshaping the inverter output admittance by alleviating the interactions between the PLL and the grid impedance [4]. However, the complete decoupling of the PLL from the grid impedance is difficult. Also, active damping feedback loops can improve small-signal stability, for example, by modifying the current reference [3] or altering the output of the current controller [14], [15]. However, these additional loops in the control structure will increase the system's complexity [16].

Recently, the redesign of the current controllers, such as the proportional-resonant (PR) controller and the proportional-integral (PI) one, has been demonstrated as a more effective solution for tackling unstable issues of GFL inverters in weak grid conditions [6], [17], [18]. It is revealed in [14] and [18] that the inverter output admittance is affected by both the PLL and the current controller in the low-frequency range. So, the small-signal stability can be improved by the inverter output admittance reshaping via tuning the current controller parameters, which offers a cost-effective solution without any reconstructing work in the control part [17], [18]. In [6], a single-input single-output transfer-function-based redesign guideline is proposed to

TABLE I
COMPARISON OF THE STATE-OF-THE-ART TECHNIQUES FOR IMPROVING SMALL-SIGNAL STABILITY

Ref.	Description	Advantages	Disadvantages	Studied SCR
[2], [11], [21]	Limiting the PLL bandwidth.	It is simple and easy to operate.	Stabilization effect sacrifices the dynamic performance.	> 1
[9]	Modifying the PLL control structure.	It can maintain a suitable PLL bandwidth.	It is troublesome and impractical for the existing inverters.	2.5
[13]	Connecting an extra inverter to the PCC.	It avoids modifying the work on the existing inverter.	Increasing cost and implementation complexity.	10
[4]	Alleviating the interactions between control loops.	It can maintain a suitable PLL bandwidth.	Complete decoupling is unattainable, and the control structure is extremely complex.	1.28
[3], [14], [15]	Using the active damping control loop.	It avoids modifying work to the PLL and keeps good dynamic performance.	More complex control structure.	1.28, 3, 5
[6], [17], [18]	Redesign of the current controller in the weak grid.	It is reliable and cost-effective without any reconstruction work in the control part.	Small-signal stability in the ultra-weak grid is not always guaranteed.	2.4, 2, 2

mitigate the side-effect of the PLL on the inverter output admittance by increasing the P gain of the current controller. However, it ignores the redesign of the I gain. Furthermore, the PI gains of the current controller from a circuit perspective are redesigned in [17] to enhance the inverter output impedance magnitude, and yet greatly degrade the internal stability margin, which may trigger the destabilization of GFL inverters. A region of current controller gains is provided in [18] based on the internal stability margin constraints and the inverter output impedance analysis. However, it requires a cumbersome trial-and-error process to ensure the stability of the GFL inverter, which relies heavily on the design experience.

Despite the varieties of current controller redesign methods that have been reported, the investigation scopes are mainly concentrated on the weak grid conditions with $2 < \text{SCR} < 10$. With the large-scale integration of renewable energy resources into the power grid, grid strength has trended to be weaker, leading to ultraweak grid conditions with $\text{SCR} < 2$ [19], [20]. In such scenarios, these methods in [6], [17], and [18] may fail to ensure the stable operation of the GFL inverters. Furthermore, the presumptive operating condition of a unit power factor (PF) for GFL inverters, as assumed in most previous studies, is also impractical [19]. Especially in a weak grid, the power transfer capacity is limited [21], and hence, a proper amount of reactive current injection (RCI) to lift the power transfer capability of the GFL inverters is recommended [19]. When the active power reference surpluses the maximum transferable active power (MTAP) or the RCI is improper, the large-signal destabilization (LSD) may be triggered due to the nonexistence of the equilibrium point (EP) in the power-angle curve or the nonconvergence system state. Therefore, the LSD risk must be excluded in the inverter-grid system before investigating the small-signal stability in an ultraweak grid [2], [8]. However, the current controller redesign methods in [6], [17], and [18] are conducted without considering the large-signal stabilities.

This article tries to simultaneously address these two issues by precluding the risk of LSD before carrying out the current controller redesign based on the small-signal stability enhancement. Feasible current references and active power reference are provided to lift the active power transfer of the GFL inverter and exclude the risk of LSD, as well as to satisfy the terminal voltage restriction. Based on this, the gains of the current controller can be redesigned by considering the worst case of the grid impedance to ensure the stable operation of the GFL inverter without lowering the PLL bandwidth. The contributions of this article are summarized as follows.

1) The RCI constraints are provided for different SCR conditions to ensure the system's ability for the state to converge to the EP and the terminal voltage, keeping an acceptable operating range. The GFL inverter with these RCI constraints can avoid the LSD risk under ultraweak grid conditions of $\text{SCR} \geq 1.1$, considering active power transfer capacity and the terminal voltage restriction.
2) The ranges for the active power reference are presented for different SCR conditions to ensure the existence of the EP and meanwhile outputting the MTAP.
3) The PR gains are redesigned by solving an established optimization problem with constraints of internal and external stabilities. During the solution process, real-time impedance detection is not required. The proposed redesign method can ensure sufficient stability margin in GFL inverters when interfaced with ultraweak grids.

The rest of this article is organized as follows. In Section II, the large-signal stability of the inverter-grid system is analyzed to prevent the LSD risk. In Section III, a small-signal model of the GFL inverter is built in the $\alpha\beta$-frame to reveal the SSD mechanisms in ultraweak grids. The redesign guideline for the PR gains is elaborated in Sections IV, and V validates the effectiveness of the proposed redesign method through simulation and experimental results. Finally, Section VI concludes this article.

II. ANALYSIS OF THE LARGE-SIGNAL STABILITY FOR THE INVERTER-GRID SYSTEM

A. Description of the Studied Inverter-Grid System

Fig. 1 illustrates the general diagram of a three-phase GFL inverter integrated into the power grid via an *LCL* filter, where L_1, L_2, and C represent the inverter-side inductor, the grid-side inductor, and the filter capacitor, respectively. In the power part, the grid impedance consists of the grid resistance R_g and the grid inductance L_g, where L_g includes L_2, transformer leakage, and line inductance $\check{L}_g$. $u_{o\,abc}$, v_{abc}, u_{abc}, $i_{1\,abc}$, and i_{abc} represent the inverter output voltages, capacitor voltages, grid voltages, inverter-side currents, and grid-side currents, respectively. The control part of the GFL inverter includes the PLL, the power control loop, and the current control loop. The synchronization

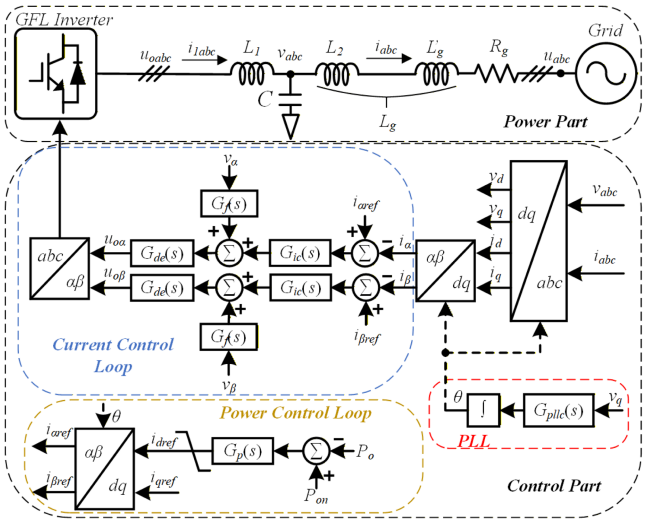

Fig. 1. General diagram of the inverter-grid system.

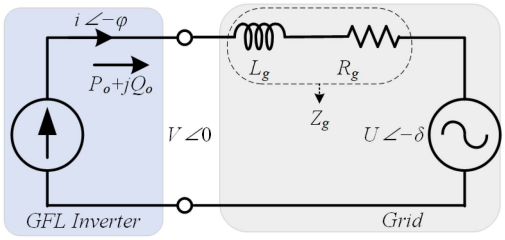

Fig. 2. Static equivalent circuit of the inverter-grid system.

signal is provided by the synchronous reference frame (SRF) PLL, which is based on the phase of v_{abc}. The power control loop generates the current references i_{ref}, where i_{dref} is derived from the active power control loop (APCL) and i_{qref} is predetermined, as described in Section II-C. Furthermore, the PWM signals of the switching devices are produced by the current control loop, where $G_{ic}(s)$ represents the current controller to eliminate the steady-state tracking error of the current reference [22] and improve the small-signal stability of the GFL inverter in this article, $G_{de}(s)$ stands for the total delay link, $G_f(s)$ denotes a bandpass filter (BPF) of the capacitor voltage feedforward (CVF) loop to suppress current startup inrush [23], which are expressed as

$$\begin{cases} G_{ic}(s) = k_{ip} + k_{ir}\frac{s}{s^2+\omega_0^2} \\ G_{de}(s) = e^{-1.5T_s s} \\ G_f(s) = \frac{\omega_{bc} s}{s^2+\omega_{bc} s+\omega_0^2} \end{cases} \tag{1}$$

where k_{ip} is the P gain of $G_{ic}(s)$, k_{ir} is the R gain of $G_{ic}(s)$, T_s is the sampling period, and ω_{bc} is the BPF bandwidth of $G_f(s)$. Note that $G_f(s)$ is a unit at the nominal angular frequency ω_0, i.e., 0 dB in the magnitude and 0° in the phase.

B. Analysis of the Large-signal Stability Conditions for the Inverter-Grid System

Fig. 2 shows the static equivalent circuit of the inverter-grid system, where the GFL inverter is regarded as a controlled current source, *the uppercase italic symbols* are the amplitudes of corresponding elements, δ denotes the power angle between V and U, and φ represents the PF angle. Using the superposition theorem, the static equation of the network is [24]

$$V_d + \mathrm{j}V_q = (R_g + \mathrm{j}X_g)\cdot(i_d + \mathrm{j}i_q) + U(\cos\delta - \mathrm{j}\sin\delta) \tag{2}$$

in the dq-frame, where X_g is the grid reactance, and subscripts d and q denote the dq-components of corresponding elements.

When the GFL inverter is in a steady state, the input error of the PLL is eliminated, i.e., $V_q = 0$ [2]. Thus, V_d and δ can be deduced from (2) that

$$\begin{cases} V_d = \sqrt{U^2 - (X_g i_d + R_g i_q)^2} - X_g i_q + R_g i_d \\ \delta = \arcsin\frac{X_g i_d + R_g i_q}{U}. \end{cases} \tag{3}$$

According to (3), the inverter's output active power P_o is calculated by

$$P_o = 0.75\frac{U^2}{X_g}\sin(2\delta) - 1.5Ui_q\sin(\delta) + 1.5R_g\left[i_q^2 - \frac{Ui_q\cos(\delta)}{X_g} + \left(\frac{U\sin(\delta) - R_g i_q}{X_g}\right)^2\right]. \tag{4}$$

The SCR is defined as [19]

$$\lambda = \frac{S_{\mathrm{ac}}}{S_n} = \frac{1.5U^2}{|Z_g|\,S_n} = \frac{1.5U^2}{X_g S_n\sqrt{1+\alpha_z{}^2}} \tag{5}$$

where λ is the SCR value, S_{ac} is the short-circuit power of the grid, S_n is the rated power of the GFL inverter, and α_z is the reciprocal of the quality factor for grid impedance, i.e., R_g/X_g.

Substituting (5) into (4), the power-angle equations of the GFL inverter can be rewritten as

$$P_o = 0.5\lambda S_n\sqrt{1+\alpha_z^2}\sin(2\delta) - 1.5Ui_q\sin(\delta) + 1.5\alpha_z\left[\begin{array}{l}\frac{1.5U^2 i_q^2}{\lambda S_n\sqrt{1+\alpha_z^2}} - Ui_q\cos(\delta) \\ +\left(\frac{\lambda S_n\sqrt{1+\alpha_z^2}\sin(\delta)}{1.5U} - i_q\alpha_z\right)^2\cdot\frac{1.5U^2}{\lambda S_n\sqrt{1+\alpha_z^2}}\end{array}\right]. \tag{6}$$

For the sake of simplicity, R_g is usually ignored as the worst-case in the stability analysis and design [25]. Let $\partial P_o/\partial\delta = 0$, yields

$$\begin{cases} \delta_m = \arccos\left(\frac{1.5Ui_q + \sqrt{(1.5Ui_q)^2 + 8(\lambda S_n)^2}}{4\lambda S_n}\right) \\ P_{om} = P_o|_{\delta=\delta_m} = S_n\cdot\left[-0.75\frac{i_q}{I_n} + 0.25\sqrt{\left(\frac{i_q}{I_n}\right)^2 + 8\lambda^2}\right] \\ \quad\times\sqrt{0.5 - \frac{\left(\frac{i_q}{I_n}\right)^2 + \frac{i_q}{I_n}\sqrt{\left(\frac{i_q}{I_n}\right)^2 + 8\lambda^2}}{8\lambda^2}} \end{cases} \tag{7}$$

where I_n is the nominal current, and δ_m presents the maximum power angle corresponding to the ideal MTAP of the GFL inverter, i.e., P_{om}. As seen in (7), both δ_m and P_{om} increase with the increasing i_q amplitude.

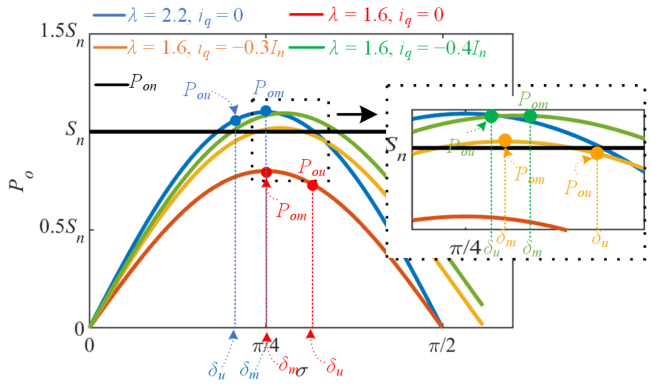

Fig. 3. P_o-δ curves in different λ and i_q conditions, where $\alpha_i = 1.25$.

Considering that every GFL inverter has an upper output current limitation to guarantee thermal safety [26], substituting this maximum output current limitation, i.e., $\alpha_i I_n$ (α_i is the current-carrying capacity [21]) into (2), yields

$$\begin{cases} \delta_u = \arcsin\left(1.5\frac{U\sqrt{\alpha_i^2 I_n^2 - i_q^2}}{\lambda S_n}\right) \\ P_{ou} = P_o|_{\delta=\delta_u} = \frac{S_n}{\lambda}\sqrt{\alpha_i^2 - \left(\frac{i_q}{I_n}\right)^2}\cdot\left[\sqrt{\lambda^2 - \alpha_i^2 + \left(\frac{i_q}{I_n}\right)^2} - \frac{i_q}{I_n}\right] \end{cases} \tag{8}$$

where δ_u represents the upper limit power angle corresponding to the upper limit output current, and P_{ou} denotes the actual MTAP of the GFL inverter considering the upper limit output current. From (8), it can be observed that δ_u decreases as the i_q amplitude increases, while P_{ou} increases at first and then decreases.

The P_o-δ curves are depicted for different scenarios in Fig. 3. As seen, the large-signal stability conditions of the inverter-grid system can be summarized as follows [2].

1) The existence of the EP, i.e., the active power reference P_{on} should be less than P_{ou}.
2) The system state converges to the EP, i.e., δ_u should be restricted below δ_m where $\partial P_o/\partial\delta > 0$.

When the SCR decreases such that the MTAP falls below $P_{\rm on}$, the inverter–grid system loses its EP, as shown in Fig. 3 by the red P_o-δ curve. A proper amount of the RCI may restore the MTAP beyond $P_{\rm on}$ and avoid the LSD [19], which is depicted in Fig. 3 by the green P_o-δ curve. However, if the amount of RCI is improper, δ_u may exceed δ_m, posing the LSD risk [2], which is depicted in Fig. 3 by the orange P_o-δ curve. Therefore, the quantum of the RCI should be carefully allocated to ensure large-signal stability.

C. Reactive Current Injection Constraints for GFL Inverter

By substituting $i_q = 0$ into (7) and (8), it follows that $\delta_m = \pi/4$ and $\delta_u = \arcsin(\alpha_i/\lambda)$. From this, it can be easily inferred that the large-signal stability condition 2) holds when $\lambda \geq 1.41\alpha_i$, which prevents the GFL inverter from the LSD risk under unit PF operation. This result coincides with the scenarios in [6], [17], and [18], where small-signal stability is sufficient for stably operating the GFL inverters without analyzing the large-signal stability. When $\lambda < 1.41\alpha_i$, a proper amount of the RCI should be applied to the GFL inverter to ensure large-signal stability. Considering the critical condition of the large-signal stability condition 2), i.e., $\delta_u = \delta_m$, and substitute it into (7) and (8), giving the minimal amplitude I_{q1} of the RCI as follows:

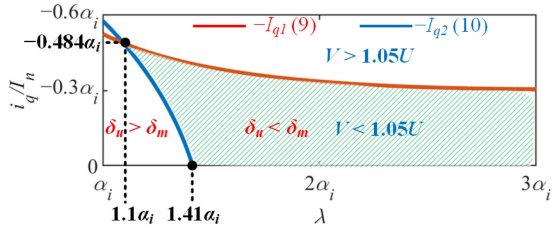

Fig. 4. Plot of i_q-λ with the constraints of (9) and (10).

$$I_{q1} = I_n\sqrt{\alpha_i^2 - \lambda^2\cdot\frac{3 - \left(\frac{\alpha_i}{\lambda}\right)^2 + \sqrt{-3 + 6\left(\frac{\alpha_i}{\lambda}\right)^2 + \left(\frac{\alpha_i}{\lambda}\right)^4}}{6}}. \tag{9}$$

In practice, the terminal voltage of the inverter-grid system is stringently restricted to a certain range for supporting an eligible service life [21], i.e., $V \leq \alpha_v U$ (α_v is the voltage restriction coefficient which is usually less than 1.05 [19]). Considering the critical condition and substituting $V = \alpha_v U$ and $\delta = \delta_u$ into (3), the maximal amplitude I_{q2} of the RCI can be obtained as

$$I_{q2} = \frac{\left|\left(1 - \alpha_v^2\right)\lambda^2 - \alpha_i^2\right|}{2\alpha_v\lambda} I_n. \tag{10}$$

Equations (9) and (10) give the range of RCI for the inverter-grid system to obey the large-signal stability condition 2) and the terminal voltage restriction rule. Fig. 4 depicts the feasible region of the RCI with the constraints of (9) and (10), where $\alpha_v = 1.05$. As shown in Fig. 4, the RCI is feasible in the green-shadow region, where $-I_{q2} \leq i_q \leq -I_{q1}$. When $\lambda < 1.1\alpha_i$, I_{qref} can only be set to $-I_{q2}$ to prevent violating the terminal voltage restriction, but violating the large-signal stability condition 2). The GFL inverter shall be operated at grid conditions of $\lambda \geq 1.1\alpha_i$ to prevent the LSD risk and obey the terminal voltage restriction rule. Notably, when $\alpha_i = 1.1$ and $\alpha_v = 1$, the weak grid conditions of $\lambda \geq 1.27$ can ensure the large-signal stability condition 2), which is in line with the result in [27].

Although the LSD risk can be prevented by lowering $P_{\rm on}$, however, low-output active power is not desired with renewable energy resources. The ability of GFL inverters to transfer higher active power is what makes them cost-effective and more meaningful. To graphically analyze the influence of the RCI on the MTAP, P_{ou} with different RCIs and λ is depicted in Fig. 5. When $\lambda > 5.41\alpha_i$, unit PF operation delivers more power and is, thus, preferable. For $1.41\alpha_i \leq \lambda \leq 5.41\alpha_i$, although the LSD does not occur, enabling the RCI is beneficial as it markedly enhances MTAP. When $\lambda < 1.41\alpha_i$, the RCI within $-I_{q1}$ and $-I_{q2}$ is mandatory to ensure large-signal stability. Therefore, $P_{\rm on}$ should be chosen from the orange-shaded region in Fig. 5 to guarantee the EP and maximize MTAP. Note that P_{ou} is below $\alpha_i S_n$ due to the terminal voltage restriction.

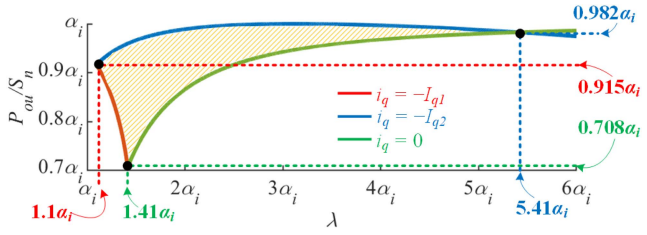

Fig. 5. Plot of P_{ou}-λ with $i_q = 0$, $i_q = -I_{q1}$, and $i_q = -I_{q2}$.

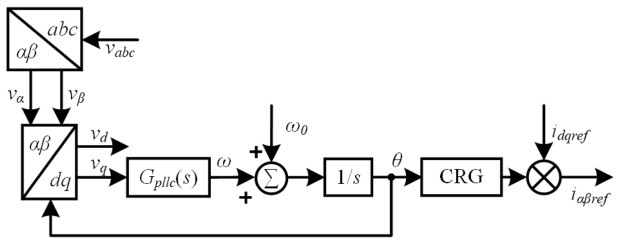

Fig. 6. Block diagram of the SRF-PLL.

III. Analysis of the Small-Signal Stability for the GFL Inverter

A. Small-Signal Modeling of the GFL Inverter

In this section, taking into account the RCI, the small-signal model of the GFL inverter is developed in the $\alpha\beta$-frame to reveal the SSD mechanisms in ultraweak grids.

First, v_d and v_q are expressed as

$$\begin{bmatrix} v_d \\ v_q \end{bmatrix} = \begin{bmatrix} \cos(\theta) & \sin(\theta) \\ -\sin(\theta) & \cos(\theta) \end{bmatrix} \begin{bmatrix} v_\alpha \\ v_\beta \end{bmatrix} \tag{11}$$

by using $\alpha\beta$-components, where θ is the PLL's output phase.

Next, imposing small-signal disturbances, θ and v are decomposed into

$$\begin{cases} v = v_0 + \Delta v \\ \theta = \theta_0 + \Delta\theta \end{cases} \tag{12}$$

where subscript $_0$ denotes steady-state values of variables and prefix Δ represents the small-signal perturbation. Considering $\cos(\Delta\theta) \approx 1$ and $\sin(\Delta\theta) \approx \Delta\theta$, and neglecting the high-order small-disturbance terms [5], (11) can be sorted into

$$\begin{cases} \Delta v_d = \Delta v_\alpha \cos(\theta_0) + \Delta v_\beta \sin(\theta_0) + \Delta\theta \cdot v_{q0} \\ \Delta v_q = -\Delta v_\alpha \sin(\theta_0) + \Delta v_\beta \cos(\theta_0) - \Delta\theta \cdot v_{d0} \\ v_{d0} = v_{\alpha 0} \cos(\theta_0) + v_{\beta 0} \sin(\theta_0) = v_0 \\ v_{q0} = -v_{\alpha 0} \sin(\theta_0) + v_{\beta 0} \cos(\theta_0) = 0. \end{cases} \tag{13}$$

Fig. 6 shows the block diagram of the SRF-PLL, where $G_{\mathrm{pll}\,c}(s)$ represents the PI controller, and the CRG denotes the current reference generator [28]. Taking the α-axis as an example, by perturbing the variables in the time-domain equations, the linearized small-signal model of the PLL can be obtained as

$$\begin{cases} \Delta\theta = \int \Delta\omega dt = \int (k_{\mathrm{pll}p} + k_{\mathrm{pll}i} \int) \Delta v_q dt \\ \Delta i_{\alpha ref} = \Delta i_{dref} \cdot \cos(\theta_0) - i_{dref0} \Delta\theta \cdot \sin(\theta_0) - i_{qref0} \\ \quad \Delta\theta \cdot \cos(\theta_0) \end{cases} \tag{14}$$

where $k_{\mathrm{pll}p}$ and $k_{\mathrm{pll}i}$ represent the proportional and integral gains of $G_{\mathrm{pll}\,c}(s)$, respectively. From (14), it indicates that the phase difference induced by the PLL dynamics is manifested through the CRG, which directly affects the production of the current references [14]. Furthermore, this disturbance current is injected into the grid, which creates a negative damping component in the inverter output admittance and may deteriorate the stability of the system. Note that i_{qref0} can be set according to (9) and (10) in an ultraweak grid.

Since i_{dref} is derived from the APCL, its linearized small-signal form can be expressed as

$$\Delta i_{dref} = -G_p(s) \cdot (v_0 \Delta i_d + i_{dref0} \Delta v_d + i_{qref0} \Delta v_q) \tag{15}$$

where $G_p(s)$ is the PI controller of the APCL. Readers can refer to [9] for more details.

Substituting (15) and (13) into (14), by applying the Laplace transform, the small-signal model of PLL in the s-domain is derived as

$$\begin{cases} \Delta v_q(s) = -\Delta\theta \cdot v_0 + 0.5\mathrm{j}\left[\Delta v_\alpha(s - \mathrm{j}\omega_0) - \Delta v_\alpha(s + \mathrm{j}\omega_0)\right] \\ \quad +0.5\left[\Delta v_\beta(s - \mathrm{j}\omega_0) + \Delta v_\beta(s + \mathrm{j}\omega_0)\right] \\ \Delta\theta(s) = \frac{G_{\mathrm{pll}c}(s)}{s} \cdot \Delta v_q(s) \\ \Delta i_{\alpha ref}(s) = -0.5 G_p(s) \\ \quad \cdot \begin{Bmatrix} v_0\left[\Delta i_\alpha(s) + \Delta i_\alpha(s + \mathrm{j}2\omega_0)\right] \\ -v_0\left[\Delta\theta(s - \mathrm{j}\omega_0) + \Delta\theta(s + \mathrm{j}\omega_0)\right] \\ +i_{dref0}\left[\Delta v_\alpha(s) + \Delta v_\alpha(s + \mathrm{j}2\omega_0)\right] \\ -\mathrm{j}i_{qref0}\left[\Delta v_\alpha(s) + \Delta v_\alpha(s + \mathrm{j}2\omega_0)\right] \end{Bmatrix} \\ \quad +\mathrm{j}0.5 i_{dref0}\left[\Delta\theta(s - \mathrm{j}\omega_0) - \Delta\theta(s + \mathrm{j}\omega_0)\right] \\ \quad -0.5 i_{qref0}\left[\Delta\theta(s - \mathrm{j}\omega_0) + \Delta\theta(s + \mathrm{j}\omega_0)\right]. \end{cases} \tag{16}$$

For the three-phase balanced inverter-grid system, $v_{\alpha\beta}$ can be expressed as

$$\begin{cases} v_\alpha = \overbrace{v_0 \cos(\theta_0)}^{v_{\alpha 0}} \overbrace{-v_0 \sin(\theta_0) \cdot \Delta\theta + \Delta v \cos(\theta_0)}^{\Delta v_\alpha} \\ v_\beta = \overbrace{v_0 \sin(\theta_0)}^{v_{\beta 0}} + \overbrace{v_0 \cos(\theta_0) \cdot \Delta\theta + \Delta v \sin(\theta_0)}^{\Delta v_\beta}. \end{cases} \tag{17}$$

According to (17), it is found that $\Delta v_\alpha = \mathrm{j}\Delta v_\beta$ [28], and thus (16) can be rewritten as

$$\begin{cases} \Delta i_{\alpha ref}(s) = \Delta i_{\alpha ref-11}(s) + \Delta i_{\alpha ref-p}(s) \\ \Delta i_{\alpha ref-11}(s) = -\overbrace{0.5 G_p(s) v_0}^{G_{p1}(s)} \Delta i_a(s) \\ \quad \overbrace{-0.5 G_p(s)\left[i_{dref0} - \mathrm{j}i_{qref0} + \mathrm{j}v_0 \cdot H_{\mathrm{pll}}(s - \mathrm{j}\omega_0)\right]}^{G_{p2}(s)} \Delta v_\alpha(s) \\ \quad + \overbrace{0.5\left(i_{dref0} + \mathrm{j}i_{qref0}\right) H_{\mathrm{pll}}(s - \mathrm{j}\omega_0)}^{T_{\mathrm{pll}}(s)} \Delta v_\alpha(s) \\ \Delta i_{\alpha ref-p}(s) = G_{p1}(s + \mathrm{j}2\omega_0) \Delta i_a(s + \mathrm{j}2\omega_0) \\ \quad +G_{p2}(s + \mathrm{j}2\omega_0) \Delta v_a(s + \mathrm{j}2\omega_0) \\ \quad \overbrace{-0.5\left(i_{dref0} - \mathrm{j}i_{qref0}\right) H_{\mathrm{pll}}(s + \mathrm{j}\omega_0)}^{T_{\mathrm{pll}p}(s)} \Delta v_\alpha(s + \mathrm{j}2\omega_0) \\ H_{\mathrm{pll}}(s - \mathrm{j}\omega_0) = \frac{\Delta\theta(s - \mathrm{j}\omega_0)}{\mathrm{j}\Delta v_\alpha(s)} = \frac{G_{\mathrm{pll}c}(s - \mathrm{j}\omega_0)}{s - \mathrm{j}\omega_0 + v_0 \cdot G_{\mathrm{pll}c}(s - \mathrm{j}\omega_0)} \end{cases} \tag{18}$$

where $H_{\mathrm{pll}}(s - \mathrm{j}\omega_0)$ is the transfer function of PLL, $\Delta i_{\alpha ref\text{-}11}(s)$ is the current reference yielding from $\Delta v_\alpha(s)$, $G_{p1}(s)$ is the transfer function from $\Delta i_{\alpha ref\text{-}11}(s)$ to $\Delta i_\alpha(s)$, $G_{p2}(s)$ is the

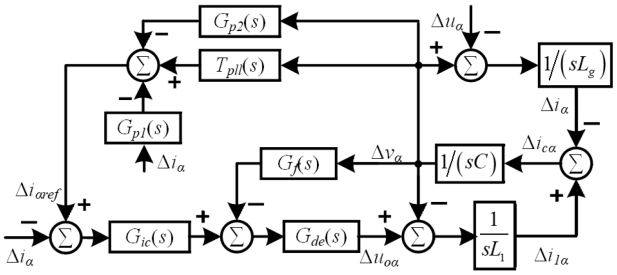

Fig. 7. Control diagram of the small-signal model for the three-phase balanced GFL inverter.

transfer function from $\Delta i_{\alpha ref\text{-}11}(s)$ to $\Delta v_\alpha(s)$ considering $G_p(s)$, $T_{\rm pll}(s)$ is the transfer function from $\Delta i_{\alpha ref\text{-}11}(s)$ to $\Delta v_\alpha(s)$ without $G_p(s)$, $\Delta i_{\alpha ref\text{-}p}(s)$ is the current reference yielding from $\Delta v_\alpha(s + {\rm j}2\omega_0)$, and all items of $(s + {\rm j}2\omega_0)$ are derived from the frequency-coupling effect (FCE) [28]. Since the FCE arises from the *dq*-rotating transformation in the control, the FCE only appears around the *dq*-rotating frequency, so that it produces an insignificant effect on the impedance characteristics of the GFL inverter [14]. For simplicity, the FCE is commonly neglected in the modeling and design analysis. Considering $\Delta i_{\alpha ref}(s) \approx \Delta i_{\alpha ref\text{-}11}(s)$, the control diagram of the small-signal model for the three-phase balanced GFL inverter is shown in Fig. 7.

Regarding $\Delta v_\alpha(s)$ as disturbance, $\Delta i_\alpha(s)$ can be expressed as

$$\begin{aligned}\Delta i_\alpha(s) &= \overbrace{\frac{G_{ic}(s)G_{de}(s)}{L_1 s + G_{ic}(s)G_{de}(s)}}^{T_c(s)}\Delta i_{\alpha ref}(s) \\ &\quad - \left[\overbrace{\frac{L_1 C s^2 + 1}{L_1 s + G_{ic}(s)G_{de}(s)}}^{Y_c(s)} + \overbrace{\frac{-G_f(s)G_{de}(s)}{L_1 s + G_{ic}(s)G_{de}(s)}}^{Y_f(s)}\right]^{Y_{ori}(s)}\Delta v_\alpha(s) \\ &= -T_c(s)G_{p1}(s)\Delta i_\alpha(s) \\ &\quad - \left[T_c(s)G_{p2}(s) + \overbrace{-T_c(s)T_{\rm pll}(s)}^{Y_{\rm pll}(s)} + Y_{ori}(s)\right]\Delta v_\alpha(s)\end{aligned} \tag{19}$$

where $T_c(s)$, $Y_c(s)$, $Y_f(s)$, $Y_{ori}(s)$, and $Y_{\rm pll}(s)$ are the closed-loop transfer function and subadmittance of the inner current control loop, subadmittance of the CVF loop, subadmittance without the PLL, and subadmittance of the PLL, respectively. All of them can be derived from Fig. 7 by applying the Mason rule. Readers can refer to [23] for more details.

According to (19), the inverter output admittance $Y_o(s)$ can be expressed as

$$Y_o(s) = -\frac{\Delta i_\alpha(s)}{\Delta v_\alpha(s)} = \frac{T_c(s)G_{p2}(s) + Y_{\rm pll}(s) + Y_{ori}(s)}{1 + T_c(s)G_{p1}(s)}. \tag{20}$$

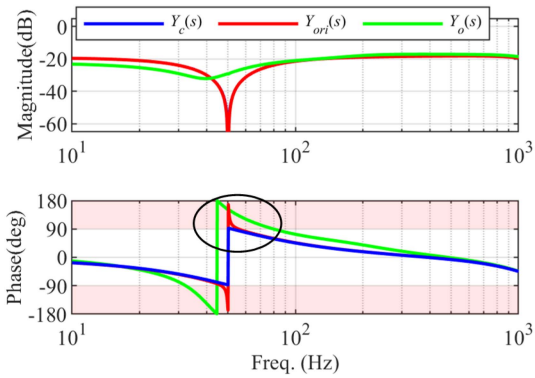

Fig. 8. Bode plot of $Y_c(s)$, $Y_{ori}(s)$, and $Y_o(s)$.

B. Stability Conditions and Admittance Characteristics

Combined (20) with $\Delta v_\alpha(s) - \Delta u_\alpha(s) = \Delta i_\alpha(s)\cdot Z_g(s)$, the overall closed-loop current response taking into account the influence of the PLL can be derived as

$$\Delta i_\alpha(s) = -\frac{Y_o(s)}{1 + Y_o(s)/Y_g(s)}\Delta u_\alpha(s). \tag{21}$$

According to impedance stability criteria, the inverter-grid system is stable if the following two conditions hold [15].

1) *Internal Stability Condition:* The GFL inverter can operate stably in a stiff grid, i.e., $T_c(s)$ is asymptotically stable.
2) *External Stability Condition:* The ratio of $Y_o(s)$ to the grid admittance $Y_g(s) = 1/Z_g(s)$ meets the Nyquist stability criterion.

If the external stability condition holds, the magnitude-phase characteristic curves of the two admittances are not intersected, or the phase margin (PM) φ_{me} at the intersection frequency f_i is larger than 0, viz.,

$$\varphi_{me} = 180^\circ - [\angle Y_o({\rm j}2\pi f_i) - \angle Y_g({\rm j}2\pi f_i)] > 0. \tag{22}$$

Since the grid impedance is mainly inductive, the phase of $Y_o(s)$ should be less than 90° at f_i to ensure the small-signal stable operation of the GFL inverter. Fig. 8 shows the Bode plot of $Y_c(s)$, $Y_o(s)$, and $Y_{ori}(s)$, where the red shadow regions indicate that the phase angle of the admittance exceeds ±90°, i.e., small-signal unstable regions. As seen, the phase of $Y_c(s)$ is always less than 90° in the low-frequency range. Although the phase of $Y_{ori}(s)$ is beyond 90° around ω_0 due to the adverse influence of the CVF loop, f_i usually does not enter these frequencies due to the small magnitude of $Y_{ori}(s)$ [18]. When the PLL is considered in the control system, $Y_o(s)$ will further extend the potentially unstable low-frequency range, which is a main cause that may lead to the SSD for the GFL inverter.

From the impedance perspective, the PLL introduces an extra low-frequency negative admittance at $Y_o(s)$, whose frequency range is widened with the increase of PLL bandwidth [5], [6]. Therefore, one simple method to enhance the small-signal stability of GFL inverters is to reduce the PLL bandwidth at the cost of degradation in the dynamic performance of the PLL. On the other hand, looking into (20), $Y_o(s)$ is affected by both the PLL and the current controller [17]. Fig. 9 shows the admittance results for different PR gains. Comparing Fig. 9(a) and (b), it

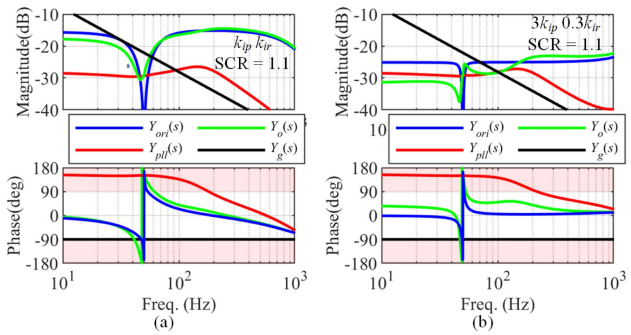

Fig. 9. Admittance results for different PR gains.

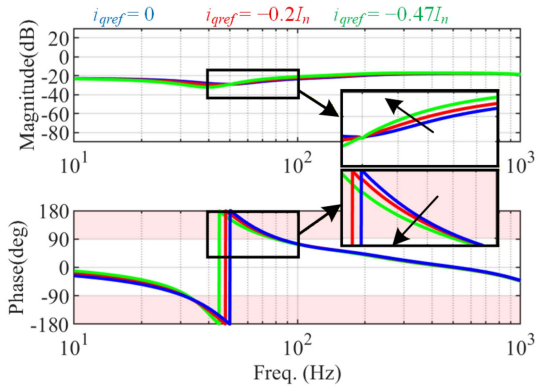

Fig. 10. Bode plot of $Y_o(s)$ with different RCIs.

can be seen that $Y_{ori}(s)$ is more affected by the redesign of the current control gains than $Y_{\text{pll}}(s)$. Therefore, these redesign methods can improve small-signal stability of GFL inverters via reshaping $Y_{ori}(s)$ to counter the side-effect of $Y_{\text{pll}}(s)$. In addition, the magnitude of $Y_o(s)$ is more affected by the retuning current controller gains than the phase of $Y_o(s)$. Hence, a more attractive alternative is to redesign the current controller gains [6], [17], [18], meanwhile keeping a wider bandwidth of the PLL, which may be conducive for the grid synchronization during the grid voltage faults.

Since the bandwidth of the APCL is typically set to around a few Hz [2], well below ω_0, the effect of the APCL on the external stability of the GFL inverter can be neglected [6]. Moreover, the effect of the RCI on $Y_o(s)$ is graphically analyzed in Fig. 10, which concentrates on the low-frequency range. Although the low-frequency small-signal stable range of $Y_o(s)$ is extended, the increased amplitude may cause f_i to shift leftward in ultraweak grids, aggravating the SSD risk.

IV. Redesign Guideline of The Current Controller

In ultraweak grids, f_i typically falls within the low-frequency range. However, an unstable low-frequency range exists for the GFL inverter owing to the negative admittance characteristics of the PLL. In this section, a redesign guideline for the current controller is presented to ensure sufficient stability margin in GFL inverters when interfaced with ultraweak grids of $\lambda \geq 1.1\alpha_i$.

A. Preselection of PR Gains Based on the Internal Stability Condition

The PR gains can be preselected using the transfer function-based frequency response method to satisfy the internal stability condition. Although this has been well-discussed in previous works [6], [23], it is briefly reviewed here for integrity.

According to (20), the inverter's open-loop transfer function $T_o(s)$ can be derived as

$$T_o(s) = G_{ic}(s)\, G_{de}(s)/(L_1 s). \tag{23}$$

Then, the PM φ_{mi} of $T_o(s)$ can be given by

$$\begin{aligned}\varphi_{mi} &= \pi + \angle T_o(\mathrm{j}\omega_c) \\ &\overset{\omega_0 \gg \omega_c \approx k_{ip}/L_1}{\approx} \frac{\pi}{2} - \arctan\left(\frac{k_{ir}}{k_{ip}\omega_c}\right) - \omega_c T_d\end{aligned} \tag{24}$$

where ω_c is the cutoff angle frequency of the current control loop. φ_{mi} is usually set from 30° to 60° to ensure that the GFL inverter has sufficient robustness and good dynamic response. According to (24), $0.06\omega_s \leq \omega_c \leq 0.1\omega_s$ is recommended, which can effectively ensure $30° < \varphi_{mi} < 60°$. To mitigate the side-effect of the resonator, $\varphi_0 = \arctan(k_{ir}/k_{ip}\omega_c)$ should be designed sufficiently small [23], typically less than 0.1. In addition, k_{ir} cannot be designed too small, which will reduce the system's tracking accuracy. Consequently, the PR gains can be preselected as

$$\begin{cases} \overbrace{0.06\omega_s L_1}^{k_{ipl}} \leq k_{ip} \leq \overbrace{0.1\omega_s L_1}^{k_{ipu}} \\ \overbrace{0.01\omega_s}^{kirl} \leq k_{ir} \leq \overbrace{0.06 k_{ipl}\omega_s \varphi_0}^{k_{iru}} \end{cases} \tag{25}$$

where k_{ipu} and k_{ipl} are the upper and lower boundaries for k_{ip}, and k_{iru} and k_{irl} are the upper and lower boundaries for k_{ir}.

B. Reselection of PR Gains Based on the External Stability Condition

In this article, the PR gains are reselected within the preselected region that developed from internal stability, to extend the fulfillment of the external stability condition in ultraweak grids of $\lambda \geq 1.1\alpha_i$. Note that if the GFL inverter is small-signal stable in the worst case of the grid impedance ($\lambda = 1.1\alpha_i$), then the external stability condition will always be kept in ultraweak grids of $\lambda \geq 1.1\alpha_i$. The reason is that when grid stiffness increases, i.e., decreasing in grid impedance, the interaction frequency of the inverter-grid system f_i will shift towards the right, viz., away from the negative admittance zone (unstable region), and PM of external stability φ_{me} will increase as λ increases. Hence, the worst case of the grid impedance, i.e., grid impedance associated with $\lambda = 1.1\alpha_i$, is selected for the further controller parameter reselection, viz.,

$$Z_g(s) = \frac{1.5U^2}{1.1\alpha_i \cdot \omega_0 S_n} s. \tag{26}$$

Based on (19), f_i can be derived from

$$|Y_o(\mathrm{j}2\pi f_i)| = |Y_g(\mathrm{j}2\pi f_i)| \tag{27}$$

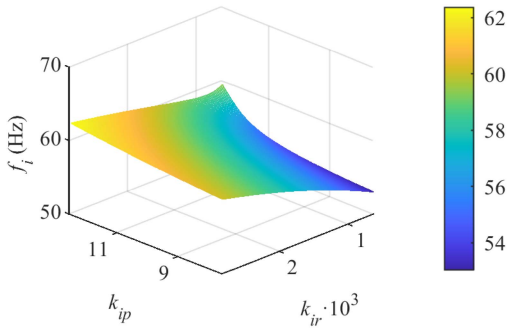

Fig. 11. Three-dimensional plot of f_i with variations of k_{ip} and k_{ir} within the preselected region.

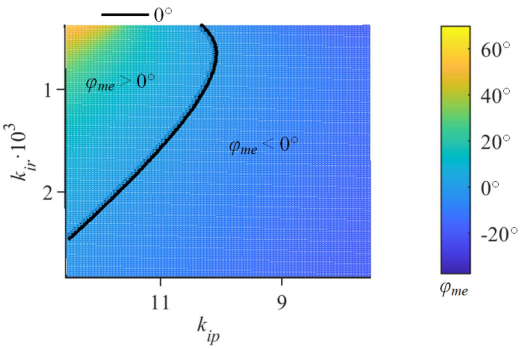

Fig. 12. Top view of 3-D plot of φ_{me} with variations of k_{ip} and k_{ir} within the preselected region.

where i_{qref} is set as $-0.484\alpha_i I_n$ to ensure the system's ability for the state to converge to the EP in ultraweak grids of $\lambda \geq 1.1\alpha_i$.

Then, it can be found from (22) and (27) that both f_i and φ_{me} are effectively tuned by adjusting k_{ip} and k_{ir}. Figs. 11 and 12 show three-dimensional (3-D) plots of f_i and φ_{me} within the preselected region, respectively. As seen in Fig. 11, f_i increases and moves away from f_0 ($f_0 = 50$ Hz) as k_{ip} rises, and the growth efficiency of f_i will be increased with the decrease of k_{ir}. As shown in Fig. 11, a larger k_{ip} and a smaller k_{ir} can ensure $\varphi_{me} > 0$, consistent with the result in [18]. However, the relationship of φ_{me} and k_{ir} is not monotonic. Simply lowering k_{ir} does not necessarily offer a higher φ_{me}.

C. Redesign Guideline

With the abovementioned analyses, the PR gains where the feasible region, i.e., $30° < \varphi_{mi} < 60°$ and $\varphi_{me} > 0$, can effectively ensure the small-signal stabilization of the GFL inverter. Therefore, the PR gains will be redesigned by establishing the following optimization problem as follows:

$$\begin{aligned} \max \quad & \alpha_w \varphi_{me} + (1-\alpha_w)\varphi_{mi} \\ \text{s.t.} \quad & k_{ipl} \leq k_{ip} \leq k_{ipu} \\ & k_{irl} \leq k_{ir} \leq k_{iru} \\ & \varphi_{me} > 0 \end{aligned} \tag{28}$$

where α_w is the weight factor of stability margins, which should be taken in the range of 0.2 to 0.8 to freely trade off the system's dynamic performance and the robustness against variations in power circuit parameters and grid impedance.

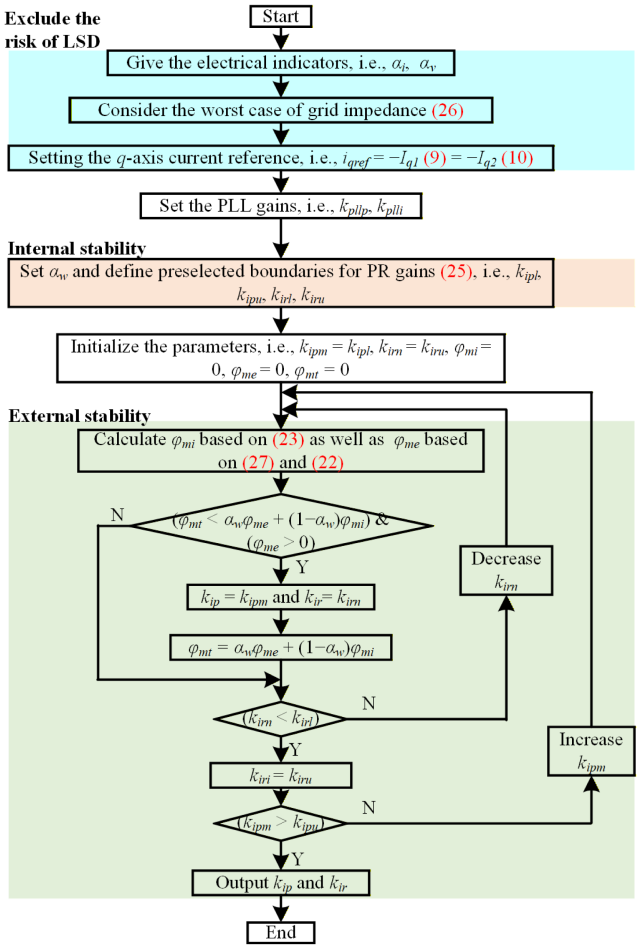

Fig. 13. Flowchart for the proposed redesign guideline of the PR controller.

Solving the above optimization problem not only achieves the stable operation of the GFL inverter in ultraweak grids of $\lambda \geq 1.1\alpha_i$, but also provides sufficient stability margins and avoids the cumbersome trial-and-error process in [18]. Fig. 13 illustrates the flowchart for the proposed redesign guideline for the PR controller, where k_{ipm} and k_{irn} are denoted as the mth k_{ip} and the nth k_{ir}, respectively. First, the q-axis current reference is set based on (9) and (10) by considering the worst case of grid impedance to exclude the risk of LSD. Second, the PR gains are preselected based on (25) to ensure the internal stability of the GFL inverter. Finally, the PR gains are redesigned by solving the optimization problem to ensure satisfactory stability margins of the GFL inverter.

D. Case Study

The power stage parameters are given in Table II, where $P_{\text{on}} = 0.9S_n$ ensures the existence of the EP. The PLL parameters are listed in Table III, where the PLL bandwidth is set as 754 rad/s.

Given that $\alpha_i = 1$ and $\alpha_v = 1.05$, λ is set to 1.1, i_{qref} is set to -3.42 A (-0.484 p.u.) to exclude the risk of LSD, and L_g is preset as 40.5 mH in (26) to account for the worst-case scenario.

TABLE II
POWER STAGE PARAMETERS

Symbol	Description	Value (p.u.)
S_n	Rated power	1.05 kVA (1)
P_{on}	Active power reference	0.945 kW (0.9)
V_{dc}	Dc-link voltage	300 V (1.73)
L_1	Inverter-side inductor	2.0 mH (0.045)
L_2	Grid-side inductor	2.0 mH (0.045)
C	Filter capacitor	3.5 μF (0.015)
f_s	Sampling/switching freq.	10 kHz (200)
U	Amplitude of grid voltage	100 V (1)
ω_0	Nominal angular freq.	314 rad/s (1)

TABLE III
CONTROLLER PARAMETERS

Symbol	Description	Value
k_{pllp}	Proportional gain of PLL	10.3
k_{plli}	Integral gain of PLL	5490
k_{pp}	Proportional gain of APCL	0.001
k_{pi}	Integral gain of APCL	0.1
ω_{bc}	BPF bandwidth	6.28
k_{ip}	Proportional gain of PR	12.57
k_{ir}	Resonant gain of PR	628

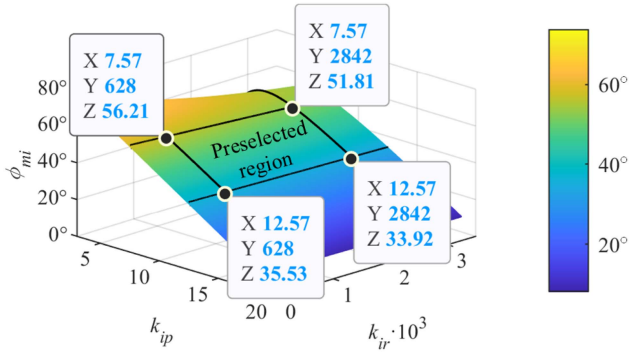

Fig. 14. Top view of 3-D plot of φ_{me} with variations of k_{ip} and k_{ir} within the preselected region.

Based on (25), the preselected region of the PR gains is [7.57, 12.57] for k_{ip} and [628, 2842] for k_{ir}, respectively. Fig. 14 shows the 3-D plot of φ_{mi} with variations of k_{ip} and k_{ir}. As seen, the preselected region of the PR gains can effectively ensure $30° < \varphi_{mi} < 60°$.

Setting $\alpha_w = 0.5$, the redesign results of the PR gains from solving the optimization problem are $k_{ip} = 12.57$ and $k_{ir} = 628$, along with $\varphi_{mi} = 35.53°$ and $\varphi_{me} = 40.27°$.

E. Comparison of Theoretical Results for Different Design Methods

In the same cases of grid condition ($\lambda = 1.1$), current references ($i_{qref} = -0.484I_n$), and active power reference ($P_{on} = 0.9S_n$), comparisons with the other redesign rules [6], [17], [18] are provided to highlight the advantages of the proposed redesign guideline. The design results of these methods are listed in Table IV. The design of k_{ip} in [6] shows a dramatically large

TABLE IV
CONTROLLER GAINS OF DIFFERENT METHODS

Symbol \ Method	Proposed	[6]	[17]	[18]
k_{ip}	12.57	450	13	12.5
k_{ir}	628	127.2	4751	11700
φ_{me}	40.2°	−53°	−14°	−32°

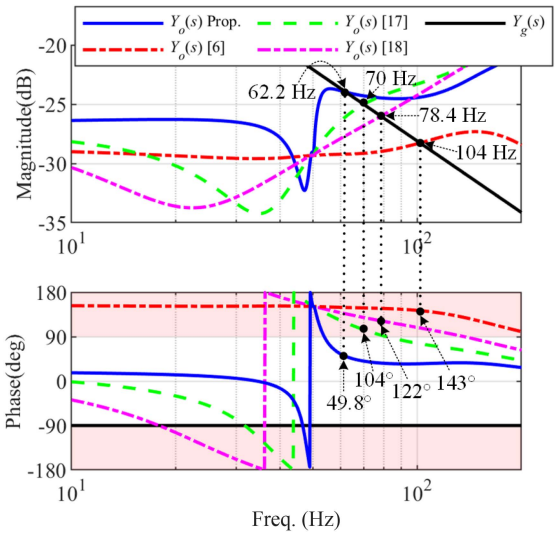

Fig. 15. Bode plot of the inverter output admittances under different design rules, where k_{ir} in [18] is set as a mid-value (11700).

result beyond its upper boundary. The design range of k_{ir} in [18] cannot always ensure the small-signal stability of the GFL inverter in $\lambda = 1.1$, resulting in a cumbersome trial-and-error process. The Bode plot of the inverter output admittances of different design rules is shown in Fig. 15. When the PR gains are redesigned using the proposed method, the phase of $Y_o(s)$ at 62.2 Hz is about 49.8° which has a large and positive PM to ensure stable operation of the GFL inverter, whereas the PMs of other design rules are all negative.

V. SIMULATION AND EXPERIMENTAL VERIFICATION

A. Simulation Verification

A time-domain simulation is built in MATLAB/Simulink to validate the effectiveness of the proposed design method. The inverter output admittance is measured via numerical simulation. The measurement procedure is referred to [29]. Fig. 16 shows the Bode plot of the theoretical and measured results. As seen, the measured output admittance is in close accordance with the theoretical one, and the GFL inverter is small-signal stable in $\lambda = 1.1$ due to $\varphi_{me} < 90°$, which confirms the correctness of the theoretical analysis.

B. Large-Signal Stability Verification Experiments

Experiments are carried out on a scaled-down GFL inverter system. The photo of the experimental setup is shown in Fig. 17, which consists of four three-phase *LCL*-type inverters, with one serving as the GFL inverter under test. The control algorithm

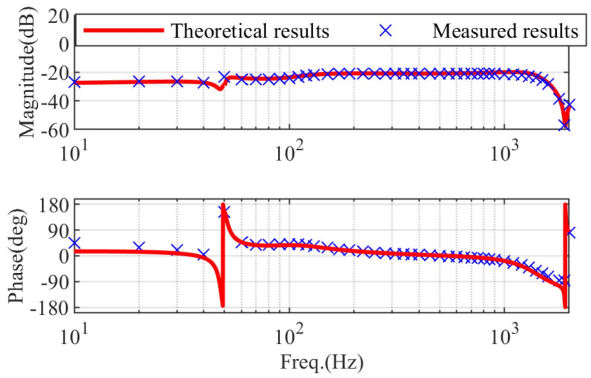

Fig. 16. Bode plot of the theoretical and measured results.

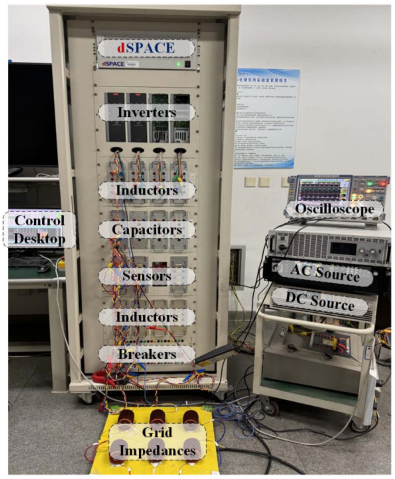

Fig. 17. Hardware picture of the experimental setup.

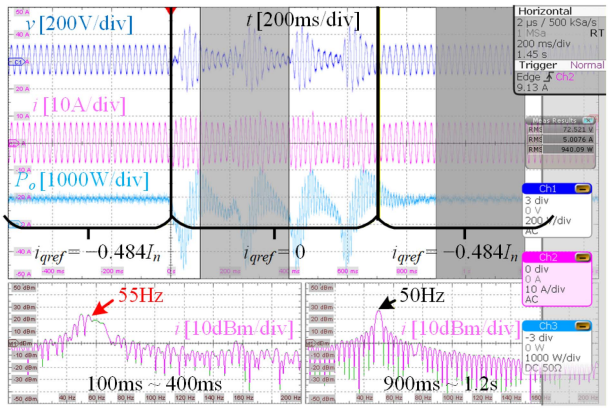

Fig. 18. Experimental waveforms under different RCIs.

is implemented on the dSPACE 1005 platform for real-time control. The discretization period of the digital controller is set equal to the sampling period.

To verify the correction of the RCI and the given P_{on} for ensuring the large-signal stability in an ultraweak of $\lambda = 1.1$, Fig. 18 shows the experimental waveforms under different RCIs. When $i_{qref} = -0.484I_n$, the GFL inverter can keep a stable

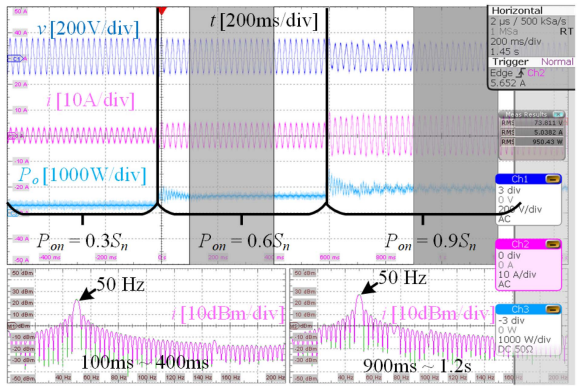

(a)

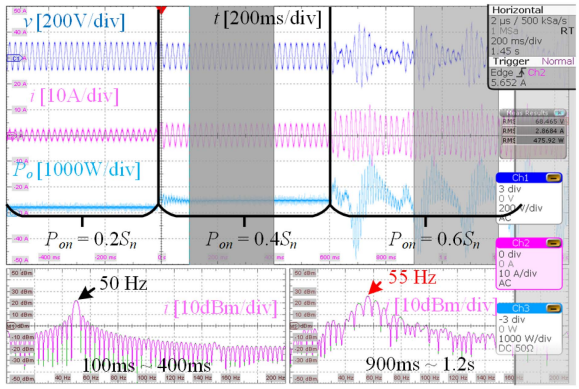

(b)

Fig. 19. Experimental waveforms in an ultraweak of $\lambda = 1.1$ with different active power references where (a) $i_q = -0.484I_n$ and (b) $i_q = 0$.

operation due to the existence of a stable EP, and the power-angle characteristic is similar to the green line in Fig. 3. When $i_{qref} = 0$, the inverter-grid system loses the EP, and the power-angle characteristic is similar to the red line in Fig. 3. Therefore, the GFL inverter suffers from the severe near-fundamental-frequency oscillation triggering the LSD, and the oscillation frequency is around 55 Hz according to the fast Fourier transform (FFT) analysis result of the current from 100 ms to 400 ms. The experimental result highlights the importance of considering large-signal stability when designing to improve small-signal stabilization of the GFL inverter. Additionally, the rms value of v in this experiment is 72.521 V, which complies with the terminal voltage restriction, and the measured P_o is 940.09 W, which is the result of ignoring grid resistance power loss and matches the expected MTAP value.

In addition, Fig. 19 shows the experimental waveforms with or without the RCI in an ultraweak of $\lambda = 1.1$ with different active power references. When $i_{qref} = -0.484I_n$, the GFL inverter can deliver power stably under different active power references. When $i_{qref} = 0$, the GFL inverter can ensure power output at active power references of 0.2 p.u. and 0.4 p.u., while the APCL loses its power synchronization control at active power reference of 0.6 p.u., resulting in LSD. The experimental results demonstrate that the developed RCI range can enhance the active power transfer capability in ultraweak grids.

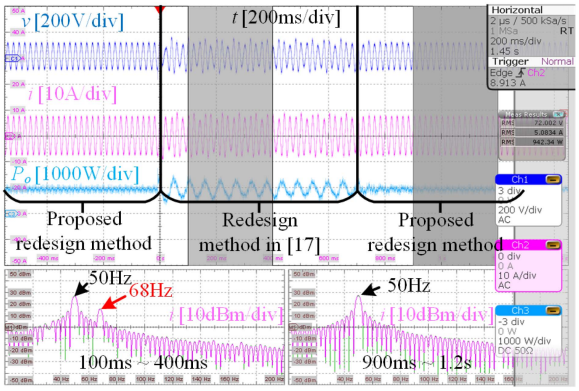

Fig. 20. Experimental waveforms in $\lambda = 1.1$ using different redesign methods.

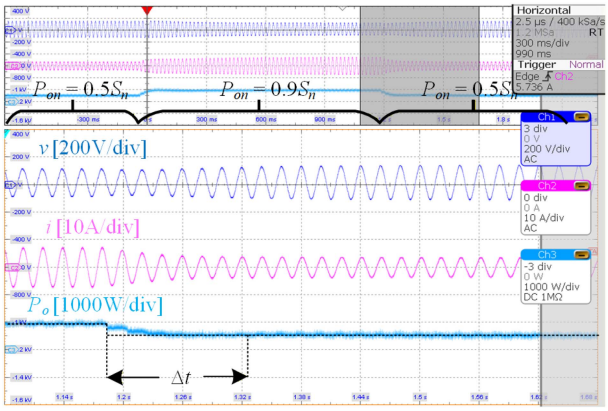

Fig. 21. Dynamic experimental waveforms in the ultraweak grid of $\lambda = 1.1$.

C. Small-Signal Stability Verification Experiments

Furthermore, to verify the effectiveness of the proposed design method for ensuring the small-signal stability of the GFL inverter in an ultraweak of $\lambda = 1.1$, Fig. 20 gives the experimental waveforms in $\lambda = 1.1$ with the proposed method and one of the state-of-the-art redesign methods having the biggest PM (see in Fig. 15). Note that both the proposed method and the comparison method use the same amount of reactive current to exclude the risk of LSD. It can be observed that the GFL inverter triggers oscillation when the PR gains are designed by the redesign method in [17]. According to the FFT analysis result of the current from 100 ms to 400 ms, the oscillation frequency is around 68 Hz, which is almost consistent with the theoretical expectation in Fig. 15. When the PR gains are redesigned by the proposed guideline, the GFL inverter returns to a stable state, as shown in the FFT analysis result of the current from 900 ms to 1.2 s. The experimental results demonstrate the effectiveness of the proposed redesign guideline in improving the small-signal stability of the GFL inverter to $\lambda = 1.1$.

D. Dynamic Experiments

Fig. 21 gives the dynamic experimental waveforms in the ultraweak grid of $\lambda = 1.1$. As seen, it takes about seven fundamental periods for the output active power to track the reference when the step change of the active power reference from 0.9 p.u. to 0.5 p.u.

VI. Conclusion

To prevent the GFL inverter from the low-frequency oscillations in an ultraweak grid, both large-signal and small-signal stabilities are taken into consideration in the control design of this article.

Through the large-signal stability analysis in terms of the power-angle curves, different large-signal stability conditions are figured out for different SCR scenarios. To be specific, when SCR $> 1.41\alpha_i$ (α_i is the current carrying capacity), the RCI is not mandatory for the absence of the LSD risks, yet the RCI is recommended since it can sharply enhance the maximum transfer active power (MTAP) of the GFL inverter; when SCR $> 5.41\alpha_i$, the unit PF operation without the RCI is more advisable since the RCI will cut down delivered capacity for the active power; when SCR $< 1.41\alpha_i$, the RCI is mandatory due to the large-signal unstable risk, the lower boundary for SCR is $1.1\alpha_i$ under the terminal voltage restriction coefficient of 1.05.

By precluding the LSD risk, an optimization problem is established to redesign the PR gains. By leveraging the optimization problem, the cumbersome trial-and-error process and real-time impedance detection are avoided, and the designed results can achieve the small-signal stable operation of GFL inverters with an enhanced MTAP under ultraweak grid conditions.

Designing a complete reactive power control structure that dynamically addresses different problems, such as active power transfer capability enhancement and reactive power compensation, would be a meaningful future work.

References

[1] Y. Xiong, H. Wu, Y. Li, and X. Wang, "Comparison of power swing characteristics and efficacy analysis of impedance-based detections in synchronous generators and grid-following systems," *IEEE Trans. Power Syst.*, vol. 40, no. 3, pp. 2545–2556, May 2025, doi: 10.1109/TPWRS.2024.3469235.

[2] P. Hu, Z. Chen, Y. Yu, and D. Jiang, "On transient instability mechanism of PLL-based VSC connected to a weak grid," *IEEE Trans. Ind. Electron.*, vol. 70, no. 4, pp. 3836–3846, Apr. 2023, doi: 10.1109/TIE.2022.3181376.

[3] F. Chen, L. Zhao, L. Harnefors, X. Wang, J. Kukkola, and M. Routimo, "Enhanced Q-axis voltage-integral damping control for fast PLL-synchronized inverters in weak grids," *IEEE Trans. Power Electron.*, vol. 39, no. 1, pp. 424–435, Jan. 2024, doi: 10.1109/TPEL.2023.3326098.

[4] X. Lin, J. Yu, R. Yu, J. Zhang, Z. Yan, and H. Wen, "Improving small-signal stability of grid-connected inverter under weak grid by decoupling phase-lock loop and grid impedance," *IEEE Trans. Ind. Electron.*, vol. 69, no. 7, pp. 7040–7053, Jul. 2022, doi: 10.1109/TIE.2021.3095791.

[5] Y. Chen, X. Ruan, Z. Lin, Y. Yan, and Y. He, "A reconstructed singular return ratio matrix for optimizing design of the PLL in grid-connected inverters," *IEEE Trans. Ind. Electron.*, vol. 70, no. 12, pp. 12453–12464, Dec. 2023, doi: 10.1109/TIE.2023.3236085.

[6] H. Gong, X. Wang, and L. Harnefors, "Rethinking current controller design for PLL-synchronized VSCs in weak grids," *IEEE Trans. Power Electron.*, vol. 37, no. 2, pp. 1369–1381, Feb. 2022, doi: 10.1109/TPEL.2021.3105549.

[7] Z. Zou, X. Liu, W. Chen, G. Buticchi, X. Wang, and M. Liserre, "Design of filter-based stabilizing control for PLL-synchronized converters," *IEEE Trans. Ind. Electron.*, vol. 71, no. 11, pp. 14208–14219, Nov. 2024, doi: 10.1109/TIE.2024.3374361.

[8] D. Dong, B. Wen, D. Boroyevich, P. Mattavelli, and Y. Xue, "Analysis of phase-locked loop low-frequency stability in three-phase grid-connected power converters considering impedance interactions," *IEEE Trans. Ind. Electron.*, vol. 62, no. 1, pp. 310–321, Jan. 2015, doi: 10.1109/TIE.2014.2334665.

[9] L. Huang et al., "Grid-synchronization stability analysis and loop shaping for PLL-based power converters with different reactive power control," *IEEE Trans. Smart Grid*, vol. 11, no. 1, pp. 501–516, Jan. 2020, doi: 10.1109/TSG.2019.2924295.

[10] X. Zhang, S. Fu, W. Chen, N. Zhao, G. Wang, and D. Xu, "A symmetrical control method for grid-connected converters to suppress the frequency coupling under weak grid conditions," *IEEE Trans. Power Electron.*, vol. 35, no. 12, pp. 13488–13499, Dec. 2020, doi: 10.1109/TPEL.2020.2991185.

[11] B. Wen, D. Dong, D. Boroyevich, R. Burgos, P. Mattavelli, and Z. Shen, "Impedance-based analysis of grid-synchronization stability for three-phase paralleled converters," *IEEE Trans. Power Electron.*, vol. 31, no. 1, pp. 26–38, Jan. 2016, doi: 10.1109/TPEL.2015.2419712.

[12] D. Zhu, S. Zhou, X. Zou, and Y. Kang, "Improved design of PLL controller for LCL-type grid-connected converter in weak grid," *IEEE Trans. Power Electron.*, vol. 35, no. 5, pp. 4715–4727, May 2020, doi: 10.1109/TPEL.2019.2943634.

[13] L. Jia, X. Ruan, W. Zhao, Z. Lin, and X. Wang, "An adaptive active damper for improving the stability of grid-connected inverters under weak grid," *IEEE Trans. Power Electron.*, vol. 33, no. 11, pp. 9561–9574, Nov. 2018, doi: 10.1109/TPEL.2018.2793242.

[14] T. Fang, H. Zhang, H. Wu, and Y. Zhang, "Robustness enhancement of coping with dual factors for grid-connected inverter in weak grid based on synthesis-admittance- phasor scheme," *IEEE Trans. Ind. Electron.*, vol. 70, no. 11, pp. 11346–11356, Nov. 2023, doi: 10.1109/TIE.2022.3231294.

[15] T. Fang, H. Liu, H. Zhang, and C. Liu, "Robust technique using the optimized grid voltage feedforward to conquer the impact induced by dual factors for grid-connected inverter in weak grid," *IEEE Trans. Ind. Electron.*, vol. 71, no. 7, pp. 7199–7209, Jul. 2024, doi: 10.1109/TIE.2023.3299011.

[16] M. Li, X. Zhang, Z. Guo, H. Pan, M. Ma, and W. Zhao, "Impedance adaptive dual-mode control of grid-connected inverters with large fluctuation of SCR and its stability analysis based on D-partition method," *IEEE Trans. Power Electron.*, vol. 36, no. 12, pp. 14420–14435, Dec. 2021, doi: 10.1109/TPEL.2021.3087028.

[17] Z. Wang, P. Cheng, H. Pan, and L. Jia, "Impedance-circuit-based stability analysis for PLL-synchronized voltage source converter in weak grid," *IEEE Trans. Circuits Syst. Regul. Pap.*, vol. 71, no. 9, pp. 4323–4336, Sep. 2024, doi: 10.1109/TCSI.2024.3415081.

[18] S. Zhou et al., "An improved design of current controller for LCL-type grid-connected converter to reduce negative effect of PLL in weak grid," *IEEE J. Emerg. Sel. Topics Power Electron.*, vol. 6, no. 2, pp. 648–663, Jun. 2018, doi: 10.1109/JESTPE.2017.2780918.

[19] D. Yang, X. Wang, F. Liu, K. Xin, Y. Liu, and F. Blaabjerg, "Adaptive reactive power control of PV power plants for improved power transfer capability under ultra-weak grid conditions," *IEEE Trans. Smart Grid*, vol. 10, no. 2, pp. 1269–1279, Mar. 2019, doi: 10.1109/TSG.2017.2762332.

[20] T. Lund, H. Wu, H. Soltani, J. G. Nielsen, G. K. Andersen, and X. Wang, "Operating wind power plants under weak grid conditions considering voltage stability constraints," *IEEE Trans. Power Electron.*, vol. 37, no. 12, pp. 15482–15492, Dec. 2022, doi: 10.1109/TPEL.2022.3197308.

[21] M. H. Ravanji, W. Zhou, N. Mohammed, and B. Bahrani, "Comparative analysis of the power output capabilities of grid-following and grid-forming inverters considering static, dynamic, and thermal limitations," *IEEE Trans. Power Syst.*, vol. 39, no. 2, pp. 2693–2705, Mar. 2024, doi: 10.1109/TPWRS.2023.3279373.

[22] M. Sanatkar-Chayjani and M. Monfared, "Stability analysis and robust design of LCL with multituned traps filter for grid-connected converters," *IEEE Trans. Ind. Electron.*, vol. 63, no. 11, pp. 6823–6834, Nov. 2016, doi: 10.1109/TIE.2016.2582792.

[23] C. Xie, K. Li, J. Zou, and J. M. Guerrero, "Passivity-based stabilization of LCL-type grid-connected inverters via a general admittance model," *IEEE Trans. Power Electron.*, vol. 35, no. 6, pp. 6636–6648, Jun. 2020, doi: 10.1109/TPEL.2019.2955861.

[24] Y. Yang, D. Zhu, X. Zou, Y. Chi, and Y. Kang, "Power compensation control for DFIG-based wind turbines to enhance synchronization stability during severe grid faults," *IEEE Trans. Power Electron.*, vol. 37, no. 9, pp. 10139–10143, Sep. 2022, doi: 10.1109/TPEL.2022.3168883.

[25] C. Wu, Y. Lyu, Y. Wang, and F. Blaabjerg, "Transient synchronization stability analysis of grid-following converter considering the coupling effect of current loop and phase locked loop," *IEEE Trans. Energy Convers.*, vol. 39, no. 1, pp. 544–554, Mar. 2024, doi: 10.1109/TEC.2023.3314095.

[26] X. Guo et al., "Analysis and enhancement of active power transfer capability for DFIG-based WTs in very weak grid," *IEEE J. Emerg. Sel. Topics Power Electron.*, vol. 10, no. 4, pp. 3895–3906, Aug. 2022, doi: 10.1109/JESTPE.2021.3089235.

[27] M. Li, X. Zhang, Z. Guo, X. Liu, Q. Chen, and M. Ma, "Grid impedance adaption dual mode grid-connected stability control strategy in a weak grid," *Acta Energiae Solaris Sinica*, vol. 42, no. 7, pp. 86–93, 2021, doi: 10.19912/j.0254-0096.tynxb.2019-0488.

[28] Q. Qian, S. Xie, J. Xu, K. Xu, S. Bian, and N. Zhong, "Output impedance modeling of single-phase grid-tied inverters with capturing the frequency-coupling effect of PLL," *IEEE Trans. Power Electron.*, vol. 35, no. 5, pp. 5479–5495, May 2020, doi: 10.1109/TPEL.2019.2946984.

[29] C. Xie, D. Liu, K. Li, J. Zou, K. Zhou, and J. M. Guerrero, "Passivity-based design of repetitive controller for LCL-type grid-connected inverters suitable for microgrid applications," *IEEE Trans. Power Electron.*, vol. 36, no. 2, pp. 2420–2431, Feb. 2021, doi: 10.1109/TPEL.2020.3014365.

Guangda Ma (Student Member, IEEE) received the B.S. degree in electrical engineering from Wenzhou University, Wenzhou, China, in 2020. He is currently working toward the Ph.D. degree in control science and engineering with the School of Automation Engineering, University of Electronic Science and Technology of China, Chengdu, China.

His current research interests include modeling and control of grid-connected inverters for renewable energy generation.

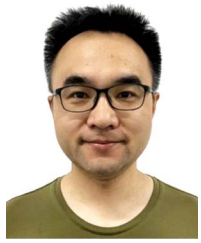

Chuan Xie (Senior Member, IEEE) received the B.S. degree in automation engineering from the University of Electronic Science and Technology of China (UESTC), Chengdu, China, and the Ph.D. degree in power electronics from Zhejiang University, Hangzhou, China, in 2007 and 2012, respectively.

Since 2012, he has been a Lecturer with the School of Automation Engineering, UESTC, where he was promoted to Associate Professor in 2019. From 2022, he is as a part-time professor with Shenzhen Institute for Advanced Study, UESTC. From May 2015 to May 2016, he was a Visiting Scholar with the Department of Energy Technology, Aalborg University (AAU). His main research interests include digital control of power electronics, grid synchronization technology, distributed generation systems, microgrids, and power quality.

Cheng Li (Student Member, IEEE) received the B.S. and M.S. degrees in automation engineering in 2020 and 2023, respectively, from the University of Electronic Science and Technology of China, Chengdu, China, where he is currently working toward the Ph.D. degree in electronic information with the School of Automation Engineering.

His current research interests include modeling and control of grid-connected inverters for renewable energy generation.

Jianxiao Zou (Member, IEEE) received the B.S., M.S., and Ph.D. degrees in control science and engineering from the University of Electronic Science and Technology of China (UESTC), Chengdu, China, in 2000, 2003, and 2009, respectively.

He is currently a Professor with UESTC, and has been the Vice Dean with the Shenzhen Institute for Advanced Study, UESTC, since 2020. He was a Visiting Scholar with the University of California, Berkeley, CA, USA, in 2010; and a Senior Visiting Professor with Rutgers, the State University of New Jersey, New Brunswick, NJ, USA, in 2014. His research interests include control theory and control engineering, renewable energy control technologies, and intelligent information processing and control.